Downstream development during ridging South Atlantic Ocean anticyclones

Thando Ndarana[1] · Lesetja E. Lekoloane[2] · Tsholanang S. Rammopo[1] · Chris J. C. Reason[3] · Mary-Jane M. Bopape[4] · Hector Chikoore[5] · Francois A. Engelbrecht[6]

Abstract

Ridging South Atlantic high pressure systems (ridging highs) are often accompanied by cut-off low (COL) pressure systems aloft, but may also occur without them, in which case a linear baroclinic wave would be observed propagating across the South African domain in the upper troposphere. Using 41 years of ERA-5 reanalysis data, this study documents differences between the characteristics of the prevailing dynamical processes and associated local eddy kinetic energy generation, its downstream transfer and dissipation during these two scenarios. The study shows that when COLs are present then baroclinic conversion is strong and it is confined east of the Greenwich Meridian, whereas it is located downstream of South Africa and it is much weaker, when ridging occurs without COLs. The differences in strength and locations of the baroclinic conversion are associated with the differing jet streak configurations between the two scenarios; which lead to Rossby wave breaking and the absence thereof when there are COLs and when ridging occurs without COLs, respectively. The presence of breaking during COLs leads to trans-ridge downstream development that facilitates energy transfer from the midlatitudes into the South African domain. When there are no COLs present, the trans-trough downstream development is stronger than it is across the upstream ridge. Barotropic conversion from eddy kinetic energy to mean kinetic energy occurs in the South African domain during COLs, but occurs much further downstream when there are no COLs during ridging highs. The difference in the characteristics identified in this study can be traced back to the differences in the potential vorticity anomaly structures, which are largely due to whether the waves break or do not during the evolution of ridging events in the South African domain.

Lesetja E. Lekoloane, Tsholanang S. Rammopo, Chris J. C. Reason, Mary-Jane M. Bopape, Hector Chikoore, and Francois A. Engelbrecht contributed equally to this work.

✉ Thando Ndarana
  thando.ndarana@up.ac.za

  Lesetja E. Lekoloane
  Lesetja.Lekoloane@weathersa.co.za

  Tsholanang S. Rammopo
  u13154402@tuks.co.za

  Chris J. C. Reason
  Chris.Reason@uct.ac.za

  Mary-Jane M. Bopape
  mm.bopape@saeon.nrf.ac.za

  Hector Chikoore
  hector.chikoore@ul.ac.za

  Francois A. Engelbrecht
  Francois.Engelbrecht@wits.ac.za

[1] Department of Geography, Geoinformatics and Meteorology, University of Pretoria, Hatfield, South Africa

[2] Department of Research and Innovation, South African Weather Service, Centurion, South Africa

[3] Department of Oceanography, University of Cape Town, Cape Town, South Africa

[4] South African Environmental Observation Network, Colbyn, South Africa

[5] Department of Geography and Environmental Studies, University of Limpopo, Sovenga, South Africa

[6] Global Change Institute, University of the Witwatersrand, Johannesburg, South Africa

1 Introduction

The subtropical South Atlantic Ocean is characterised by a quasi-stationary anticyclonic circulation that exhibits pronounced variability in intensity and position at intra-annual and inter-annual (Sun et al. 2017) and multi-decadal (Reason 2000) time scales. This circulation may potentially be impacted by future climate change (Engelbrecht et al. 2009; Reboita et al. 2019) and therefore expected to change at decadal and centennial time scales. Under certain stratospheric conditions (Ndarana et al. 2018), the anticyclone extends east and ridges around the South African landmass to induce an onshore flow into the country (Ndarana et al. 2021a). This eastward extension process is referred to as ridging. Ridging South Atlantic Ocean high pressure systems (hereafter referred to as ridging highs) draw moisture from the South Atlantic and Southwest Indian Oceans (Rapolaki et al. 2020) by means of geostrophic and ageostrophic moisture fluxes (Ndarana et al. 2021a) and, by so doing, contribute to the moisture budget of the country. These oceans are, however, not the only sources of moisture for South Africa, because water vapour may originate from the Equatorial South Atlantic Ocean (Vigaud et al. 2007) and Equatorial Indian Ocean (D'Abreton and Tyson 1995) and transported into tropical Africa. The Angola low (Reason and Jagadheesha 2005; Crétat et al. 2019; Howard and Washington 2018) then organises it in a south easterly direction (Hart et al. 2010) and tropical/extra-tropical interaction events then transport the moisture further south (Ratna et al. 2013; Macron et al. 2014) into South Africa.

Ridging highs are consequently important in terms of the dynamics of rain-producing weather systems of South Africa because they are low level processes that co-occur with moving troughs (Piva et al. 2008; Ndarana et al. 2022) that may develop into cut-off low (COL) pressure systems (Taljaard 1985; Singleton and Reason 2007) when the waves break (Ndarana and Waugh 2010; Reyers and Shao 2019; Barnes et al. 2021). Heavy rainfall that sometimes leads to floods which cause extensive damage to property and loss of life often results from ridging highs that occur in tandem with COLs (Trigaardt et al. 1988; Singleton and Reason 2006; Pinto et al. 2022). Moreover, ridging highs may also be associated with tropical-temperate troughs (Hart et al. 2010) whose characteristic outgoing longwave radiation anomaly pattern (Fauchereau et al. 2009) being negative and reaching maximum values as the ridging process matures (Ndarana et al. 2021a). It follows then that understanding the dynamics associated with this process at both the lower and upper levels may play an important role in informing predictability studies of extreme rainfall events in the South Atlantic Ocean/South African sector.

One approach that previous studies have employed in understanding upper level dynamical processes is the local energetics framework (Orlanski and Katzfey 1991) to diagnose the evolution of baroclinic waves (Orlanski and Sheldon 1995), which gives rise to the notion of downstream development (Orlanski and Sheldon 1993, 1995). The local energetics framework has since been applied to a broad range of atmospheric dynamical settings, beyond the evolution of baroclinic waves, including intensifying jet streaks (Lackmann et al. 1999), surface cyclolysis (McLay and Martin 2002), life cycles of conservative extratropical cyclones that exhibit explosive deepening behaviour (Decker and Martin 2005), extratropical transitions of tropical cyclones (Harr and Dea 2009), travelling mid-tropospheric troughs (Piva et al. 2010), the evolution of cut-off low (COL) pressure systems (Gan and Piva 2013, 2016; Ndarana et al. 2021b; Pinheiro et al. 2022), dynamical processes that lead to the formation of frost events (Müller et al. 2017), the processes that maintain jet wave trains (Li 2021) and dust storms (Rivière et al. 2015); to name a few. Some studies (e.g. Lackmann et al. 1999; Danielson et al. 2006) have also linked the energetics framework with wave activity fluxes. It might therefore find some applications to upper level dynamical processes that are associated with ridging pressure high systems as well, as these processes are baroclinic waves.

Ndarana et al. (2022) showed that there are at least two types of ridging high evolution that occur in the South African domain. These were categorised according to which latitude they occur, relative to the 40°S latitude line. Type-S (Type-N) ridging events occur south (north) of this latitude line. They also showed that the different types of ridging highs are associated with baroclinic waves aloft, whose troughs pass over South Africa as the ridging process is initiated. Whilst other studies (e.g. O'Brien and Reeder 2017) have analysed the evolution of these waves in the South Atlantic Ocean/South African sector using their interaction with the jet as a basis for their analysis; little is known about the dynamical characteristics of these waves in the South African domain from a downstream development perspective. Recent studies (e.g. Ndarana et al. 2021b; Pinheiro et al. 2022) showed that COLs are characterised by such downstream development, which is facilitated by ageostrophic geopotential fluxes that draw eddy kinetic energy from the mid-latitudes into the COL's formation region. This in turn induces the closed cyclonic circulation of the COL, together with the effect of the high potential vorticity (PV) anomaly that does the same (Hoskins et al. 1985). This high PV anomaly is normally caused by Rossby wave breaking (RWB), defined as the rapid and irreversible overturning of PV contours which was first identified during boreal winter stratosphere (McIntrye and Palmer 1983). RWB has been shown in the upper troposphere to be associated with COLs (Ndarana

and Waugh 2010; Reyers and Shao 2019; Portmann et al. 2021; Barnes et al. 2021) and rainfall (de Vries 2021).

It is well known from forecasting experience in southern Africa that COLs are often accompanied by ridging highs at the surface, but the opposite is not necessarily true. This is expected to be the case as Ivanciu et al. (2022) showed that 44% of ridging highs are associated with RWB events. It follows then that as not all RWB cases are associated with COLs (Ndarana and Waugh 2010; Barnes et al. 2021), it may then be expected that even fewer ridging highs will have COL association. When COLs do occur in the domain, the associated RWB events are observed somewhere in the region near the Greenwich Meridian to about 25°E and they often have an anticyclonic orientation either with an equatorward (Thorncroft et al. 1993) or a poleward (Peters and Waugh 1996) bias. In this study the proportion of ridging highs that are associated with COLs will be quantified.

Given this, there are many instances when ridging highs occur with ordinary trough/ridge systems aloft that do not exhibit the wave breaking that is observed during COLs. Piva et al. (2010) analysed the energetics of such troughs in the South American domain and found that the presence of the Andes mountains amplifies the troughs as they propagate across the land and affects the energetics. In the South African domain, where the mountains are much lower than the Andes, only the energetics of COLs have been considered (Ndarana et al. 2021b) and therefore the effect of the absence of breaking baroclinic waves that lead to isolated potential vorticity anomalies (or cutoffs) has not been considered yet. As such the questions raised in the study are

- How does the absence of COLs (and associated RWB) affect the upper level dynamical processes as the linear baroclinic waves propagate through the South Atlantic Ocean/South African sector during the evolution of ridging highs?
- Do the prevailing upper level ridging highs dynamical processes lead to different eddy kinetic energy generation, transfer and dissipation?

The questions raised above will complement recent energetics studies in the South African domain (Ndarana et al. 2021b) and the Southern Hemisphere in general (Pinheiro et al. 2022) by considering the case of linear baroclinic wave energetics that might lead to rainfall over South Africa due to their association with the ridging process.

The rest of the paper is structured as follows: in the next section a brief review of the energetics diagnostic framework is presented, followed by Data and Methods in Sect. 3. The results are presented in Sect. 4 and the Concluding remarks are given in Sect. 5.

2 Review of flow processes and downstream development in baroclinic waves

To characterise downstream development, the variables of interest are first divided into their basic state and perturbation parts, where the former are represented by capital letter symbols with a subscript m and the perturbation fields are the small letters so that the instantaneous horizontal velocity and geopotential fields are separated into their basic state and perturbation portions as $\mathbf{V} = \mathbf{V}_m + \mathbf{v}$ and $\Phi = \Phi_m + \phi$, respectively. The horizontal flow may be decomposed into its zonal and meridional components as $\mathbf{V} = U\mathbf{i} + V\mathbf{j}$ and the three dimensional flow is represented by $\mathbf{U} = \mathbf{V} + \omega\mathbf{k}$, where ω is the vertical velocity in pressure coordinates, so that $\mathbf{u}$ becomes its perturbation. Note that $\mathbf{i}, \mathbf{j}$ and $\mathbf{k}$ are unit vectors in the zonal, meridional and vertical directions, respectively. On this basis, the eddy kinetic energy is defined as $K_e = \frac{1}{2}\mathbf{v} \cdot \mathbf{v}$ and the flux form (Orlanski and Sheldon 1993; McLay and Martin 2002) of the equation that describes its evolution is then given by

$$\partial_t K_e = - \nabla_p \cdot (\mathbf{V}K_e) - \partial_p(\omega K_e) - \mathbf{v} \cdot \nabla_p \phi$$
$$- [\mathbf{v} \cdot (\mathbf{u} \cdot \nabla_p)\mathbf{V}_m] + \text{Residual} \quad (1)$$

The first and second terms on the right hand side of Eq. (1) are the horizontal and vertical eddy kinetic energy flux convergence, respectively. The third term can be interpreted as the advection of the perturbation geopotential field by the horizontal perturbation velocity field. The fourth term is the Reynolds stress term, which is the conversion of K_e to mean kinetic energy and the "Residual" is obtained by subtracting the terms just described from $\partial_t K_e$. In all these terms the subscript p indicate that the horizontal gradient and divergence operators are evaluated on isobaric surfaces. Note that $\nabla_p(\cdot)$ and $\nabla(\cdot)$ are the two and three dimensional gradient operators, respectively, so that $\nabla(\cdot) = \nabla_p(\cdot) + \mathbf{k}\partial_p(\cdot)$. The pressure work term, $\mathbf{v} \cdot \nabla_p \phi$, plays a dominant role in this eddy kinetic energy budget equation and various processes are embedded in it (Orlanski and Katzfey 1991). These processes are most clearly seen when it is decomposed in the following manner,

$$-\mathbf{v} \cdot \nabla_p \phi = -\omega\alpha - \nabla_p \cdot (\mathbf{v}\phi)_a - \partial_p(\omega\phi) \quad (2)$$

Here $\alpha = -\partial_p \phi$ and the rest of the symbols have already been defined. Once decomposed, it becomes clear that $-\mathbf{v} \cdot \nabla_p \phi$ is a dominant term in Eq. (1) because it embodies all the K_e generation processes. The first term on the right-hand side, $-\omega\alpha$, is the baroclinic conversion, which when it is positive (i.e. $-\omega\alpha > 0$), represents the conversion from eddy available potential to eddy kinetic energy. There clearly needs to be vertical motion so that baroclinic conversion is essentially facilitated by vertical heat fluxes (Li 2021). The

second term is the convergence of ageostrophic geopotential flux of K_e which is a horizontal process and the fluxes themselves, $(\mathbf{v}\phi)_a$, as represented by the red curved arrows in Fig. 1, serve to radiate energy in the direction of the ageostrophic flow, across a ridge axis, so that a downstream, K_e, may then develop at the inflection point immediately east of the ridge axis. Across a trough axis, the downstream directed ageostrophic flux is caused by the fact that the flow is subgeostrophic (with a ageostrophic flow directed upstream) and $\phi < 0$. The term $\partial_p(\omega\phi)$ is the vertical geopotential flux convergence, and it is considered small when the fields are vertically integrated from 1000 hPa to 100 hPa.

Based on Orlanski and Sheldon (1995) for baroclinic waves in general and for the COL case in the South Atlantic Ocean/southern African sector (Ndarana et al. 2021b) and Southern Hemisphere in general (Pinheiro et al. 2022),
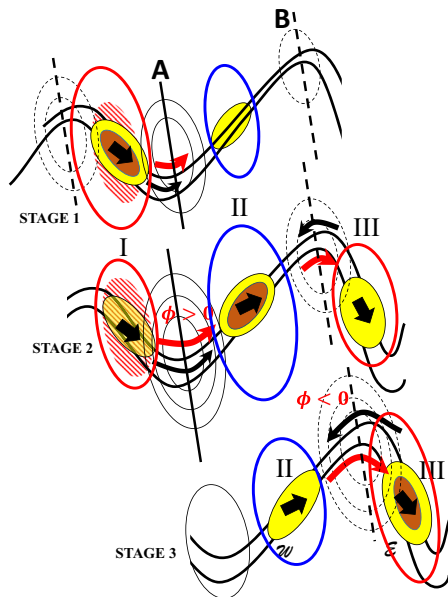
Fig. 1 Shematic representation of a propagating baroclinic wave (black curves) together with its evolving eddy kinetic energy (K_e) density centres (yellow and brown shaded oval shapes and labelled in Roman numerals I, II and III—the brown shade represents increasing strength of eddy kinetic energy) and geopotential perturbation (ϕ) patterns (oval shapes with no shading. The thin black solid (dashed) contours represent area in the wave where $\phi > 0$ ($\phi < 0$). The black curved arrows represent the ageostrophic flow ($\mathbf{v}_a$) and the red curved arrows represent the ageostrophic geopotential fluxes ($\mathbf{v}_a\phi$). The solid (dashed) straight line marked as A (B) represent the ridge (trough) axis. The increasing size of the arrows ($\mathbf{v}_a$, $\mathbf{v}_a\phi$) and increasing number of contours (K_e, ϕ), represent increasing intensity of these fields. The red (blue) unshaded oval shapes represent areas in the baroclinic wave where the perturbation meridional velocity field is negative (positive). The hacthed region in eddy labelled I represent baroclinic conversion from eddy available potential energy to eddy kinetic energy ($-\omega\alpha > 0$). [The schematic is adapted from Orlanski and Sheldon (1995) but also draws from the findings of Ndarana et al. (2021b) and Pinheiro et al. (2022) for COLs in the South Atlantic Ocean/southern African sector and Southern Hemisphere, respectively.]

downstream development is a three stage process. During the first stage a K_e centre I is generated by means of baroclinic conversion ($-\omega\alpha > 0$), as represented by the red hatched oval shape in Fig. 1. At the bottom of the wave, across the ridge axis, the supergeostrophic flow, as represented by the downstream directed ageostrophic flow, combined with $\phi > 0$, combine to produce the ageostrophic geopotential fluxes that begin to transport K_e downstream. As K_e I decreases in strength from stage 1 to stage 2, K_e II increases in strength to reach a maximum during the latter. This may largely be due to the increase in positive perturbation geopotential anomaly in the ridge and the perturbation ageostrophic flow, thus increasing transport of energy downstream via the ageostrophic geopotential fluxes, which are particularly strong in COLs. This strength is caused by anticyclonically breaking waves which induce deep geopotential anomalies and a strong supergeostrophic flow ahead of the closed circulation (Ndarana et al. 2021a; Reyers and Shao 2019; Ndarana et al. 2021b). The negative perturbation field across the trough axis (downstream of energy centre II) begins to appear and the upstream ageostrophic flow lead to energy transfer toward the inflection point beyond the trough axis to cause K_e III to develop. As was the case with the strengthening ridge, as the trough deepens, the flux increases; thus increasing K_e centre III.

3 Data and methods

3.1 Data

We use the Fifth Generation European Centre for Medium-Range Weather Forecasts Reanalysis (ERA5, Hersbach et al. 2020) products from 1979 to 2020. The horizontal grid spacing of each dataset is 2.5° at 6-hourly time intervals. Even though these products are available at finer mesh grids than this, we deem the chosen grid spacing sufficient because ridging high pressure systems are synoptic scale processes, the horizontal scale of which is $\sim 10^6$ m (Holton and Hakim 2014). The variables used are mean sea level pressure (MSLP), the zonal and meridional wind components and geopotential heights to calculate the geostrophic($v_g\mathbf{i} + v_g\mathbf{j}$) and ageostrophic ($v_a\mathbf{i} + v_a\mathbf{j}$) wind fields at standard pressure levels. In this study we assumed a variable f geostrophic flow (Blackburn 1985) so that it is not non-divergent (Cook 1999). Unlike other reanalysis products, ERA5 comes with potential vorticity (PV), which is a derived field from the flow and potential temperature. In order to linearly interpolate PV from isobaric to isentropic surfaces, the later is calculated directly from the temperature output.

3.2 Methods

We objectively identify ridging highs using a simple algorithm consisting of three steps. Its details are provided in Ndarana et al. (2018) and only a brief description of it is provided here. In the first step, closed contours in the 6-hourly MSLP fields are identified within a domain bounded by 40°W and 60°E. We then group these closed contours so that concentric contours in the South Atlantic Ocean represent the South Atlantic Ocean High (SAOH). This is the second step. In the third and final step, if the outermost contour extends east of the 25°E longitude line, we record such instances as the ridging process having occurred. If this condition is met on consecutive time steps, without any breaks in between, then this constitutes a single ridging event and is the basis on which the duration of the events is determined.

We also identify COLs at the 250 hPa isobaric level using the method of Barnes et al. (2021). In the first step closed contours at 1 gpm geopoential intervals and their centres are identified and concentric contours are grouped together, in a similar fashion as the ridging high identification algorithm discussed above. This step produces closed circulations, that may be cyclonic or anticyclonic, whose centres are considered to be the mean of the longitudes and latitudes of the concentric contours. To discard the former, each of these centres are then required to be 10 gpm lower than at least 6 of the surrounding 8 grid points on a 2×2 grid box, so that the retained closed circulations are low pressure systems. To impose the closed core condition, we employ the 250–500 hPa thickness, which was found in Ndarana and Waugh (2010) to perform better than temperature fields. If the thickness at the centre of the circulation is lower than at least 5 of the surrounding 8 grid points, then the cold core condition is considered to have been met. Following Barnes et al. (2021), gaps are filled. After tracking the COL events, if two of them occur within 12 h and 500 km of one another, these are considered to be the same event. As in Singleton and Reason (2007), COLs that affect South Africa are considered to be those that occur within the grid box bounded by 10°E and 40°E, and 20°S and 40°S for at least 24 h.

To establish the climatological behaviour of the ridging events and associated fields, we calculate composite means. To understand the energetics associated with these events more clearly, we isolate cases when these occur without COLs and compare them to cases when the former occurs in the South African domain. To do this, for each ridging event we search for a COL that occurs during the evolution of the former. If no COL is found, then we group the ridging events as "ridging without COLs". Composites for this group are then generated using the duration of the ridging events as the only basis for the calculations. Corresponding times during the evolution of the ridging events are brought together and averaged. For instance, all the fields occurring at the time step that ridging occurs (e.g. t = 0 h) occurs are averaged, then those at the second time step are brought together and averaged (t = +6 h) and so on. The COL events are further sub-divided into groups that occur in four quadrants of the South African domain, following Singleton and Reason (2007) and refer to these as south-western, north-western, north-eastern and south-eastern sub-regions (see cf. Fig. 1 in Singleton and Reason 2007). Following the categorisation, the same procedure of calculating composites is followed, but using the day of COL formation as t = 0 hrs instead of that of the ridging highs. The reason for this is to bring out the characteristics of the COLs more clearly so that a clearer comparison between the two categories of events may then be possible. The statistical significance of the composite anomaly fields is established following Brown and Hall (1999).

The diagnostics described in Sect. 2 are first calculated for each COL and ridging event and then composited in the manner just described. As noted in that section, the variables are decomposed into their basic state and perturbation components. In this study, the basic state variables are defined as the 31-day mean for each event, centred on the first time that COLs and ridging events without COLs are identified. Note that all the energetics diagnostics are integrated vertically from 1000 to 100 hPa, as previous studies have done, unless otherwise stated.

4 Results

4.1 General baroclinic wave characteristics

A total of 2423 ridging events were objectively identified during the study period and 21% (497 events) of these occurred when there are COLs aloft. This proportion is less than that observed for RWB (Ivanciu et al. 2022) for reasons already mentioned in Sect. 1. As noted in Sect. 3.2, the COLs that occur with ridging are subdivided into four categories, according to where they occur in the South African domain and 212, 107, 102 and 76 of them were located in the south-western, north-western, north-eastern and south-eastern quadrants of the domain, respectively. In all the composite figures shown, for brevity only the south-western COLs events are presented in the left panels. This quadrant is also of particular interest since it contains twice as many events as any of the other quadrants and because COLs here play an important role in helping to mitigate severe winter drought (De Kock et al. 2021). The results shown below are broadly similar between events in each quadrant, with only a few small differences in the composite structure and evolution of the MSLP fields. Note that in all the figures, the left hand panels composites are presented with t = 0 hrs corresponding to the day of the formation of the closed circulation of

the COL and on the right panels t = 0 hrs corresponds to the first time that ridging occurs.

To illustrate the differences between the circulation patterns when ridging highs occur with COLs and when they occur without COLs aloft, Fig. 2 shows the 340 K PV field represented by the thin black contours for the entire isentropic surface. The PV fields were chosen over the geopotential heights because of the former's better ability to show the undulations more clearly to illustrate wave breaking (as the contours turn back on themselves). As noted in Peters and Waugh (1996), this process is most clearly seen by examining PV on isentropic surfaces. Another added advantage for using PV is that the location of the closed PV anomaly relative to the dynamical tropopause is more readily observed, which is more intuitive than the geopotential heighs, in a dynamical sense. The evolution of the PV on the left and right panels of Fig. 2 shows that the amplitude of the trough (equatorward disturbance east of the thick black curve) grows more rapidly when there are COLs aloft, than when there are no COLs. In former case it actually grows into non-linear regimes, with the PV contours turning back on themselves indicating RWB. This is clearly indicated by the north-western/south-eastern orientation of the trough axis, meaning that the perturbation horizontal flow has a strongly negative zonal component in the midlatitudes, just upstream of the South African mainland (Fig. 2b). This demonstrates that there are significant differences in the circulation patterns aloft between the two scenarios.

As noted in Sect. 1, the overall aim of this study is to characterise downstream development in the South Atlantic Ocean/Southern African domain during ridging high pressure systems, by contrasting upper level dynamics when COLs occur aloft and when ridging events are not associated with COLs. Composites of the COL events were calculated for the sub-regions referred to in Sect. 3.2 but only the evolution of composite fields associated with south western COLs are shown in the left panels of all the figures presented in the paper. South western COLs were chosen because they have the highest frequency of occurrence than in the other three quadrants, as noted above. Furthermore, many high impact COLs (e.g. Thoithi et al. 2023) are first identified here and then propagate eastward to impact the eastern coast. In Fig. 3 the MSLP (shaded), geopotential height anomalies (thin solid and dashed black contours representing positive and negative anomalies, respectively) and PV = −2.5 PVU (thick blue contours), PV = –3 PVU (thick red contours) and PV = −3.5 PVU (thick black contours) on the 340 K isentropic surface, are shown from time lags t = –24 h to t = +48 h, in 24 h intervals. Note that we use PV on the 340 K isentropic surface in the case of south-western and south-eastern COLs and on the 360 K isentropic surface for the other two categories. Note also that the anomalies are calculated as the difference between the total variables and

the 31-day mean centred on the day of the events. In using the 31-day mean as the basic state flow, this study follows previous studies (e.g. Orlanski and Katzfey 1991). Using daily climatologies of the variables would not change the patterns that have been observed in the study. During the evolution of the COLs (left panels in Fig. 3), the positive geopotential height anomalies are stronger across the ridge axes where there is clear PV overturning, indicating RWB. The negative geopotential height anomalies east of the PV overturning region are weaker but exhibit characteristics of a reflected Rossby wave, which were also observed in O'Brien and Reeder (2017) in the different context of PV based interactions of the waves with the jet stream. These observations apply to all categories of COLs (not shown). The wave breaking is deeper for southern COLs, in particular the ones upstream. This has implications for energy transfer as Gan and Piva (2013), Ndarana et al. (2021b) and Pinheiro et al. (2022) all showed that downstream development is most significant across the breaking ridge, because of the combined strength of the supergeostrophic flow (see Sect. 2 and Fig. 1) and the geopotential height anomalies found in that component of the baroclinic wave.

In contrast, the evolution of the baroclinic waves during ridging high pressure systems that do not have COLs associated with them (right panels of Fig. 3) have a stronger negative geopotental height anomalies across the trough axis (dashed contour in Fig. 3e) than the trailing positive geopotential height anomaly field, and attain absolute maximum values at time lag t = 0 hrs. This signals the inception of the ridging process. The waves that manifest under these circumstances are linear because they neither break nor is there any PV intrusion of significance. This difference in the characteristics of the baroclinic wave structure between instances when COLs occur and when there are no COLs during the ridging process is the first indication that there would be significant differences between downstream development processes associated with the two atmospheric situations. Whilst there are also differences at the surface, with the MSLP anomalies associated with south-western and south-eastern COLs showing much stronger values, all the waves exhibit a baroclinic structure, as they lag westward with height.

4.2 Dynamical processes associated with the wave trains

A place to start in explaining the possible dynamical processes that cause the differences described in the previous section are the meridional vertical structures of PV and geopotential height anomalies. These are shown in Fig. 4 as shaded fields and thin black contours, respectively, plotted with PV = –2 PVU (thick dashed blue contour) to indicate where the dynamical tropopause might be located. The PV
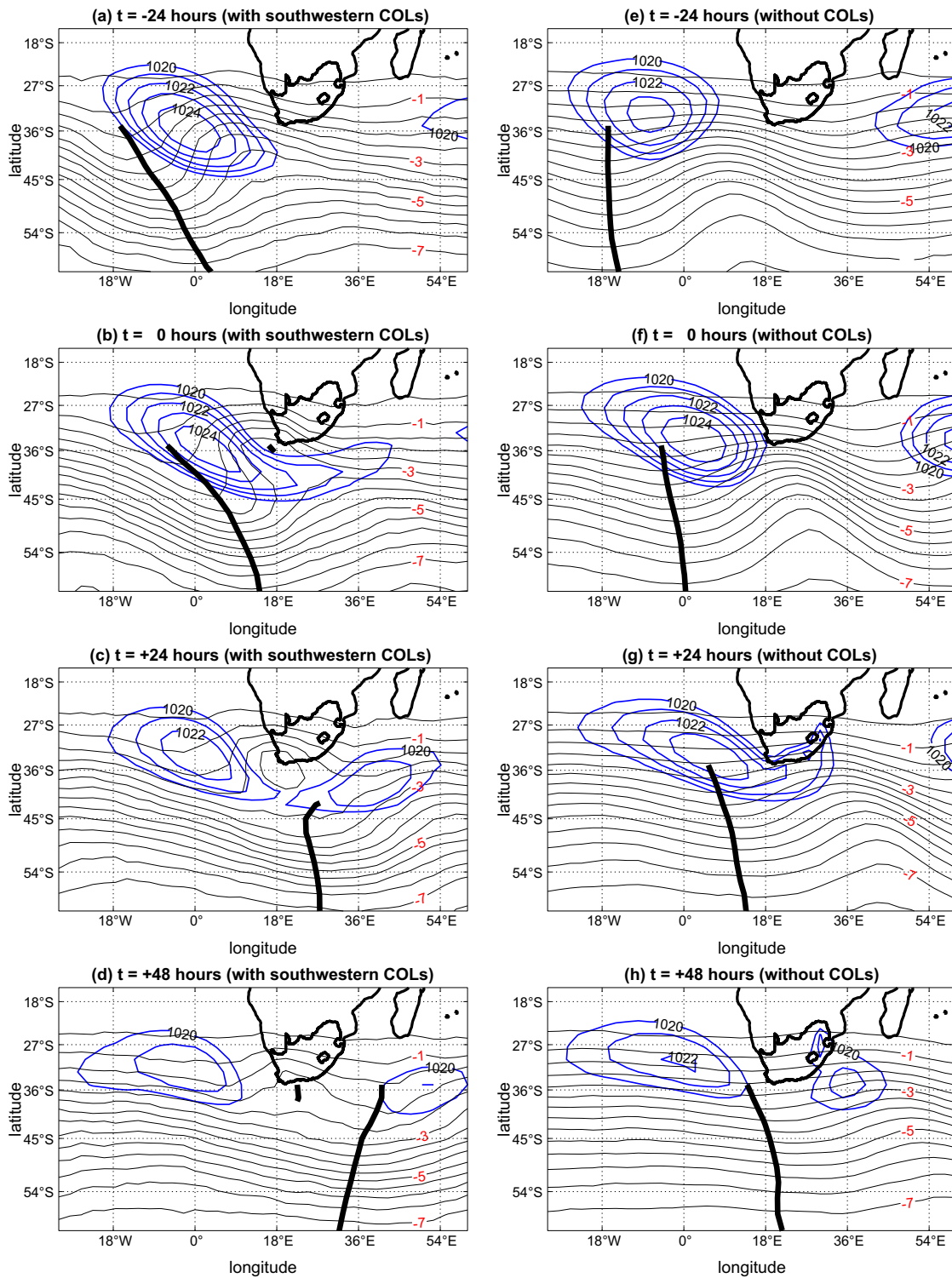
Fig. 2 Composite evolution of potential vorticity fields (thin black contours) on the 340 K isentropic surface plotted at 1 PVU contour intervals and MSLP (thick blue contours) plotted at 1 hPa and showing isobars from 2020 to 2024 hPa for ridging highs with south-western COLs (left panels) and without COLs (right panels). The com- posites are plotted from (**a, e**) t = − 48 h to (**d, h**) t = + 48 h at 24 h intervals. The thick solid black curve is included to highlight the the ridge axis that approached the South African domain across the South Atlantic Ocean
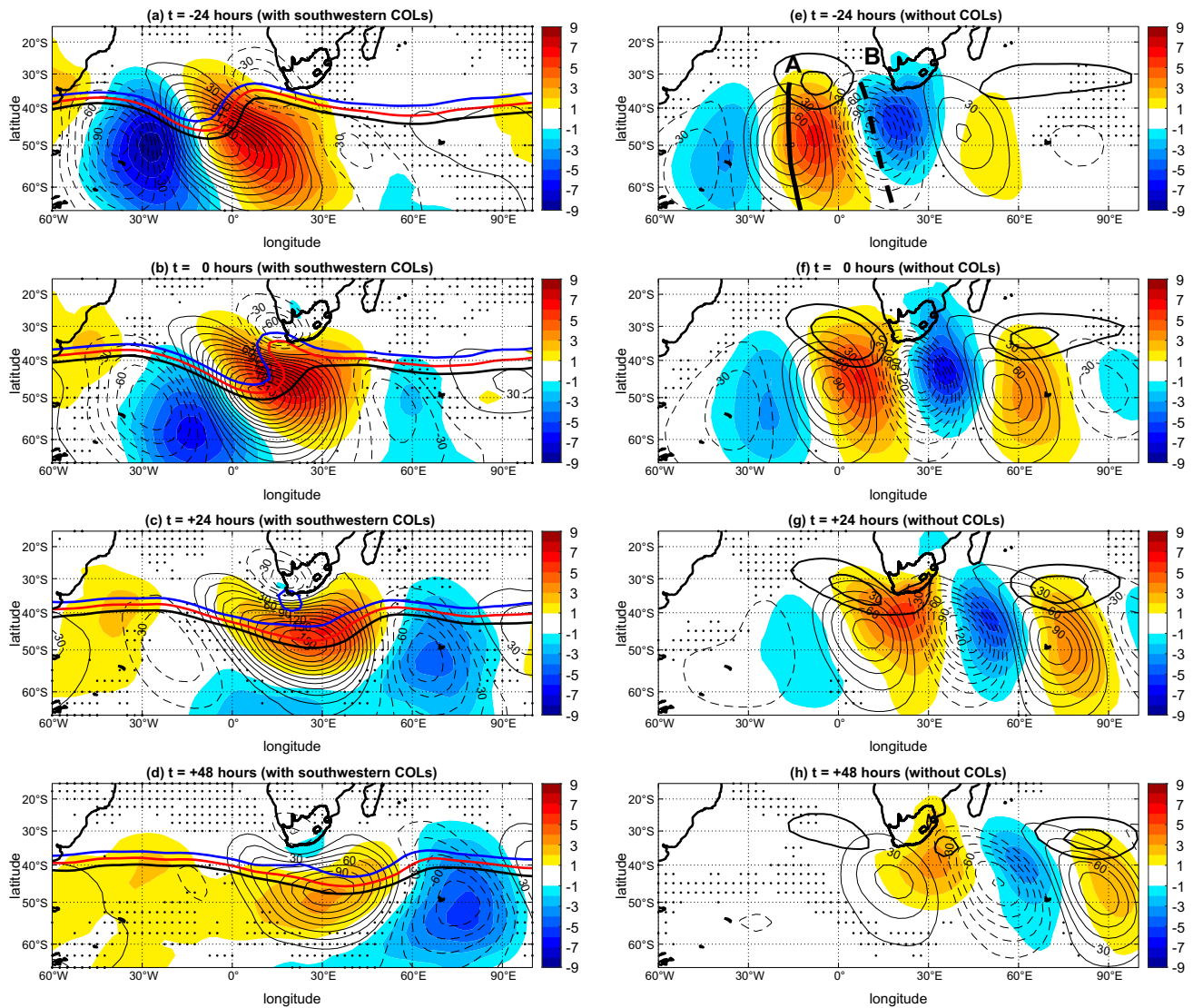
Fig. 3 Same as in Fig. 2 but positive (thin solid contours) and negative (thin dashed contours) geopotential height anomalies at the 250 hPa isobaric level, MSLP anomalies (yellow and brown (blues) shading representing positive (negative) values) and PV = −2.5, − 3 and −3.5 PVU contours, represented by the thick blue, red and black

contours, respectively. The geopotential height anomalies are plotted at 15 gpm intervals. The PV contours are plotted on the 340 K isentropic surface. The thick solid (dashed) black curves in (e) labelled A and B are the ridge and trough axes, as shown schematically in Fig. 1. Areas where there no dots are significant at the 95% confidence level

anomalies of interest are marked with capital letters A, B and C in the top panels of this figure. The geopotential height anomalies are the circulation response to the PV anomalies, which is anticyclonic and cyclonic for positive and negative anomalies, respectively; by the invertibility principle (Hoskins et al. 1985; Davis and Emmanuel 1991; Røsting and Kristjánsson 2012). As in Fig. 3, the left panels show composite evolution of these fields for south-western COLs and the right panels show the evolution of fields associated with ridging events when there are no COLs aloft, plotted for the same time lags as in Fig. 3.

Consistently with the deformation of the PV contours in Fig. 3, the south-western COLs exhibit higher

positive PV anomalies, which can be seen by comparing the eddies labelled B in Fig. 4a and e. This in turn leads to deeper geopotential height perturbation fields that also more clearly extend to the surface for southern COLs. This is consistent with the stronger surface response that is observed for COLs (left panels of Fig. 3) noted previously. Also consistent with Fig. 3, is the fact that the fields associated with eddy B are stronger than those associated with eddy C, for all COL categories. The opposite is seen when ridging occurs without COLs. The right panels of Fig. 4, and in particular at t = 0 h, show that the negative anomaly downstream at C is stronger than the positive one at B. This is the case right through the evolution of ridging

Fig. 4 Same as in Fig. 2 but for composites of meridional vertical profiles of positive (thin black solid contours) and negative (think black dashed contours) geopotential height anomalies, PV anomalies (shaded) and the PV = –2 PVU (thick blue dashed contour). The thick solid red and blue contours represent $v = -3$ m s^{-1} and $+3$ m s^{-1}, resepctively. Only PV anomalies significant at the 95% level are shown and the PV anomalies of interest are labelled A, B and C
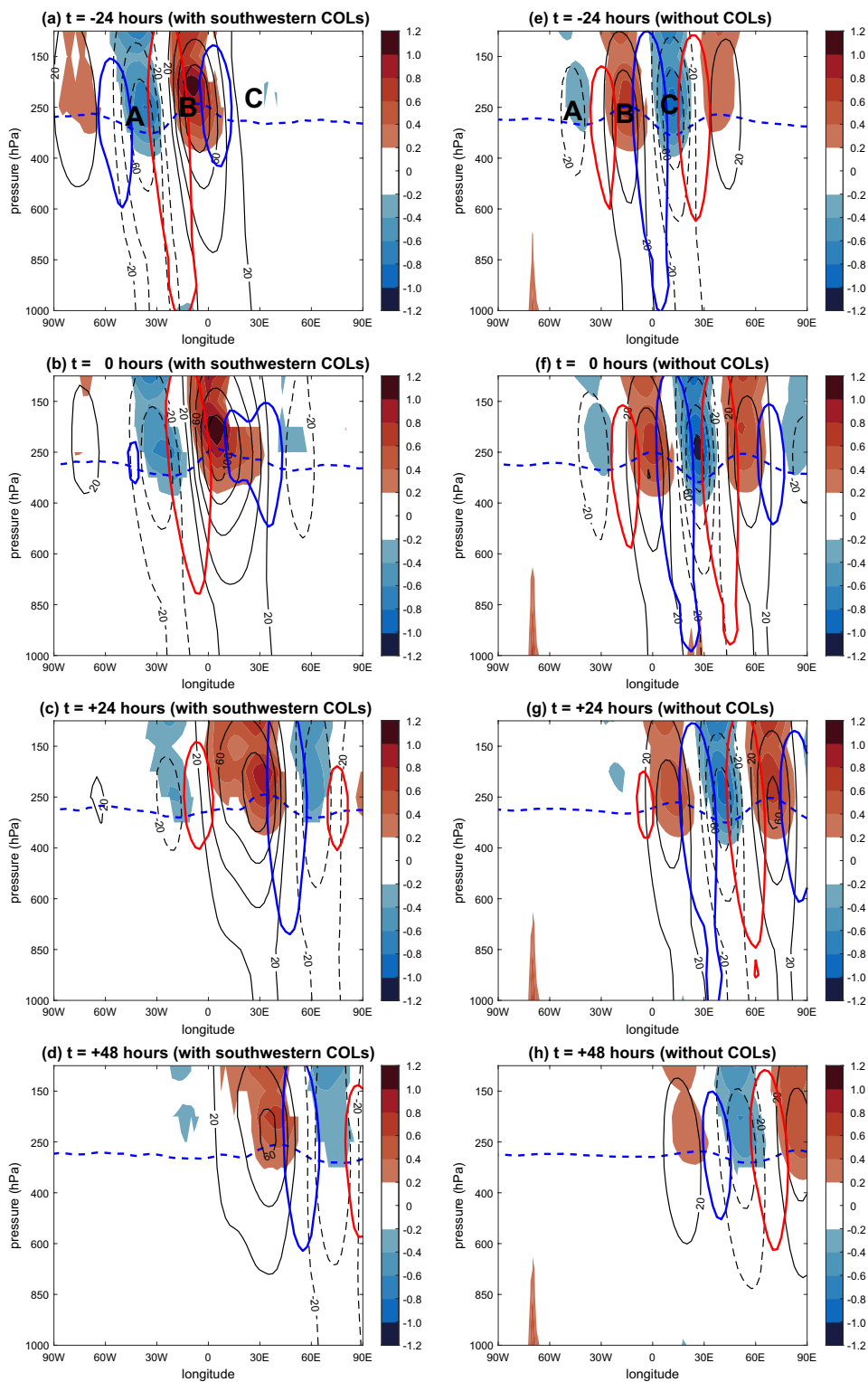

highs and most clearly seen at t = 0 h (Fig. 4f). Another difference to note between the left and right panels of Fig. 4 is that the COL PV perturbation fields are broader (larger zonal extent) than that which the upper level waves associated with ridging events with no COLs exhibit.

Therefore a stronger perturbation flow and associated eddy kinetic energy during COLs aloft can be expected.

To explain the likely cause of the breaking waves indicated by the overturning PV contours in Fig. 3b and the differences in the PV anomaly structures, we make use of

the structures of the zonal flow. Figure 5 shows zonal iso-tachs (thin black contours) that are larger than 35 m s^{-1} to highlight jet streaks, the meridional perturbation velocity $v = -3$ m s^{-1} (thick red contours) and $v = 3$ m s^{-1} (thick blue contours), which, as indicated schematically in Fig. 1, show the structure of the baroclinic waves, with the ridge axes indicated by the thick solid black curve. Note that the baroclinic eddies of interest are labelled with Roman numerals I, II and III and that in the right panels there is a fourth component of the baroclinic wave labelled IV. The shading represents the magnitude of strain calculated using $(\sqrt{2}a)^{-1} \mid \partial_\phi u + u \tan \phi \mid$ (Akahori and Yoden 1997). Early idealised modelling experiments of RWB processes (e.g.

Nakamura and Plumb 1994) showed that increasing the rate of strain causes RWB to occur. As such, the left panels of Fig. 5 show that when COLs occur in the South African domain, the baroclinic waves break anticyclonically as the magnitude of strain increases and becomes largest at t = 0 hrs (Fig. 3b on the anticyclonic side of the jet. The strain rate, in turn is caused by the presence of the jet streaks which strides the ridge axes. Note that the axes have a pronounced north-western/south-eastern tilt, as would be expected in an anticyclonically breaking wave. In clear contrast, the corresponding jet streak in the right panels of Fig. 5 is much weaker, and the associated magnitude of strain is much weaker. It is therefore expected that the likelihood of RWB
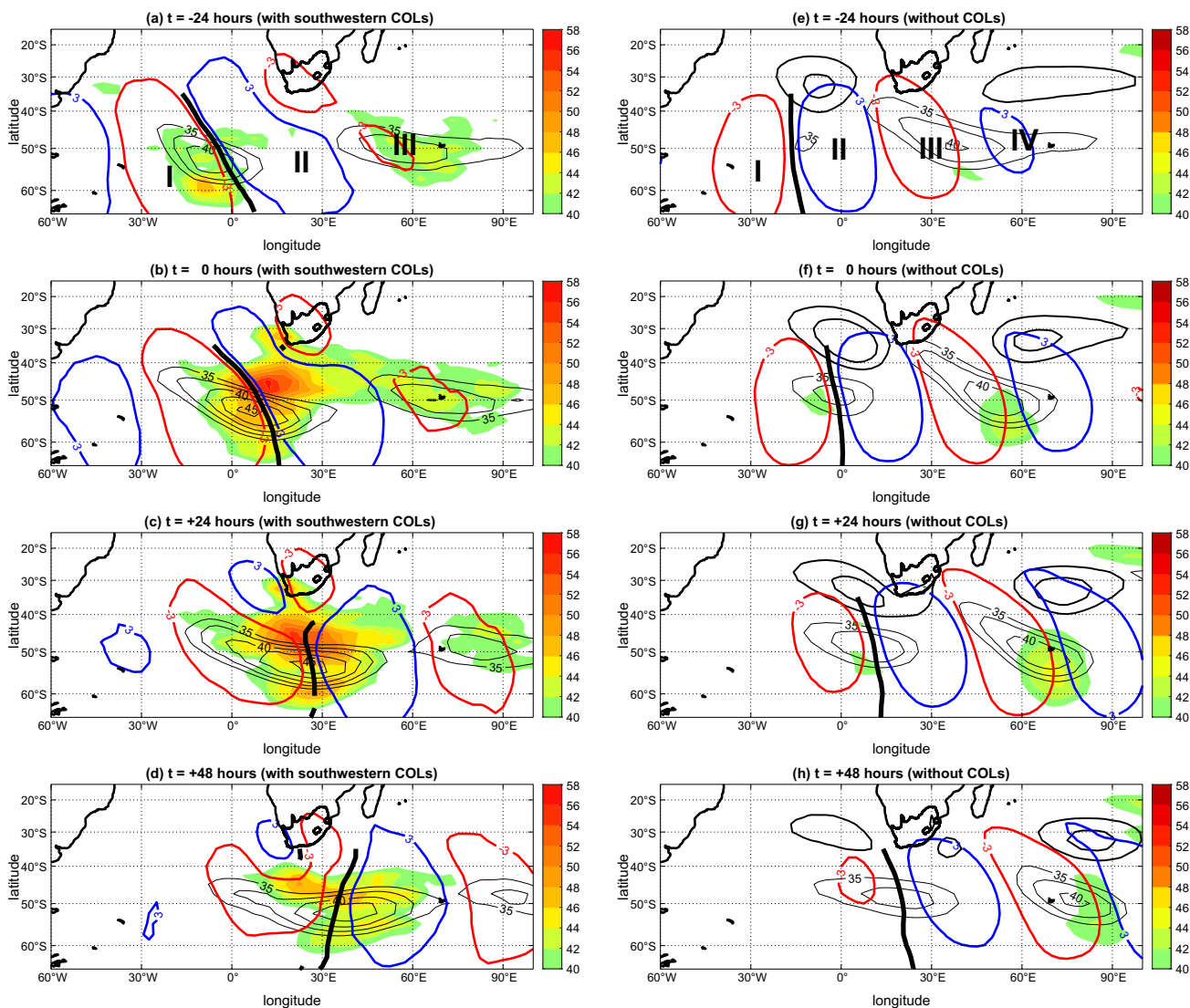
Fig. 5 Same as in Fig. 2 but for the magnitude of strain (shaded) plotted in 10^6 s^{-1}, zonal isotachs (thin black solid contours) plotted in 2.5 m s^{-1} contour intervals.The thick solid red and blue contours represent $v = -3$ m s^{-1} and $+3$ m s^{-1}, resepctively, as in Fig. 4. The thick black curve on each panel represents the location of the ridge

axis (referred to at the reference ridge in the main text), Marked A in Figs. 1 and 2. The components of the baroclinic wave that propagate past the South African domain during ridging are labelled with Roman numerals I, II and III in the top panels. In the right panels the eastern most eddy is labelled IV

occurring diminishes significantly. This explains the differences between the strength of the positive PV anomalies marked B in all the panels of Fig. 4.

It is well known from classic jet streak theory (Keyser and Shapiro 1986) that the cyclonic jet entrance region is characterised by a negative vorticity anomaly field. So, the fact that the relatively stronger downstream jet, which, according to these composite calculations, is more pronounced when there are no COLs extends back to the trough axis means that it induces a stronger negative vorticity anomaly there, and its associated PV anomaly. This stems from the fact that the cyclonic entrance of a jet streak is characterised by a negative vorticity anomaly field. A stronger negative PV anomaly results in the part of the wave marked C in the right panels of Fig. 4.

The three dimensional view of the dynamical processes involved here that are presented in Figs. 3, 4 and 5 show that there are significant differences in upper tropospheric dynamical processes during ridging highs in the South African domain when COLs are present and they are not present. We may then expect that there would be differences in the energy generation and the transfer thereof and these will be discussed next.

4.3 The eddy kinetic budget

We now discuss the spatial structure of K_e and consider the terms that contribute to its rate of change according to Equation (1). The spatial distribution of K_e is shown in Fig. 6 as shaded fields, together with statistically significant **v** (thick grey) vectors, which indicate the statistical significance at the 95% confidence level of the K_e fields, and the $U = 40 \text{ m s}^{-1}$ (very thick black contours) isotach to highlight the position of the jet streaks. Again, the eddies of interest are marked I, II and III in both the top left and right panels of Fig. 6 and eddy IV is shown in the latter. The dynamical processes discussed in the previous sections clearly have implications for the distribution and evolution of K_e in Fig. 6. Figs. 3, 4, and 5 all show that there are marked differences in the upper level dynamical characteristics during ridging high pressure systems where there are COLs and no COLs present. These differences also manifest in the eddy kinetic energy fields shown in Fig. 6. In particular, the perturbation PV fields induced by the more clearly defined RWB leads to a stronger perturbation flow for COLs located in the southern quadrants, so the eddy kinetic energy is relatively higher for these COLs as well. As it was the case with the other fields, there are marked differences between the left and right panels of Fig. 6. The stronger K_e field is located in eddy I during COLs, but it is located in component III for the case of ridging events that have no COLs associated with them. This is caused by the differences in the PV anomaly structure presented in Fig. 4, in which the negative

PV anomaly is stronger than in the COL case, thus inducing a stronger perturbation flow in eddy II (left panels of Fig. 6). Note also that K_e IV also grows beyond $t = 0$ hrs.

Ndarana et al. (2021b) showed that the kinetic energy in eddy I is converted from eddy available potential energy, as the jet streak (see left panels of Fig. 5) propagates across the South Atlantic Ocean, causing a strong eastward energy flux, thus translating the energy centre in the same direction of the movement of the midlatitude jet streak. Pinheiro et al. (2022) confirmed that this conversion is located upstream of the PV overturning region, and that it is stronger for strong COLs. Pinheiro et al. (2022) also noted that this conversion, which, according to Eq. 1., means that $-\omega\alpha > 0 \Rightarrow \partial_t K_e > 0$, occurs in the thermally direct circulation region of jet streaks. Figure 7a shows that this is the case because according to these calculations, baroclinic conversion is concentrated in eddy I, which Figs. 5 and 6 show to be co-located with the jet entrance. Note that, as in previous figures, Fig. 7a is for south-western COLs. When COLs are not present, there are two jet streaks, but the one upstream is much weaker thus the weaker conversion values in eddies I and II in Fig. 7b. The presence of the relatively strong downstream jet in the right panels of Fig. 5 and also in the context of eddy kinetic energy in Fig. 6 leads to the baroclinic conversion in eddy III in Fig. 7b, which is weaker than that which is observed for COLs because the associated jet is also weaker. Thus the thermally direct transverse circulation would also be weaker. Note that in this case this process is concentrated beyond the inception of the ridging process in eddy II at around 40°E, whereas in the COL case, it is located upstream of the Greenwich Meridian. Note also that Fig. 7b shows that there is some baroclinic conversion in eddies I and II, even though it is weak, and again, consistent with the weak upstream jet streak.

Baroclinic conversion constitutes one aspect of the pressure work term (see Eq. 2). The other aspect is the ageostrophic geopotential convergence term. As Ndarana et al. (2021b) and Pinheiro et al. (2022) note, the downstream transfer of K_e by means of ageostrophic geopotential flux is most clearly seen across the ridge (i.e. thick black curve between eddies I and II, shown in Fig. 5). This curve corresponds to the black solid line which schematically shows the ridge axis in Fig. 1. Note that the orientation of the flux divergence/convergence and the flux vectors themselves is such that energy is transported from the midlatitudes into the South African domain. This energy is transferred from eddy I into II. This, of course, is due to the wave breaking which induces a strong supergeostrophic flow across the ridge axis. When the flow is combined with the strong geopotential anomalies (see Fig. 5 and the associated discussion in the previous sections) produces a strong ageostrophic geopotential flux. Because the waves do not break in the right panels of Fig. 8, the ageostrophic fluxes across the ridge are
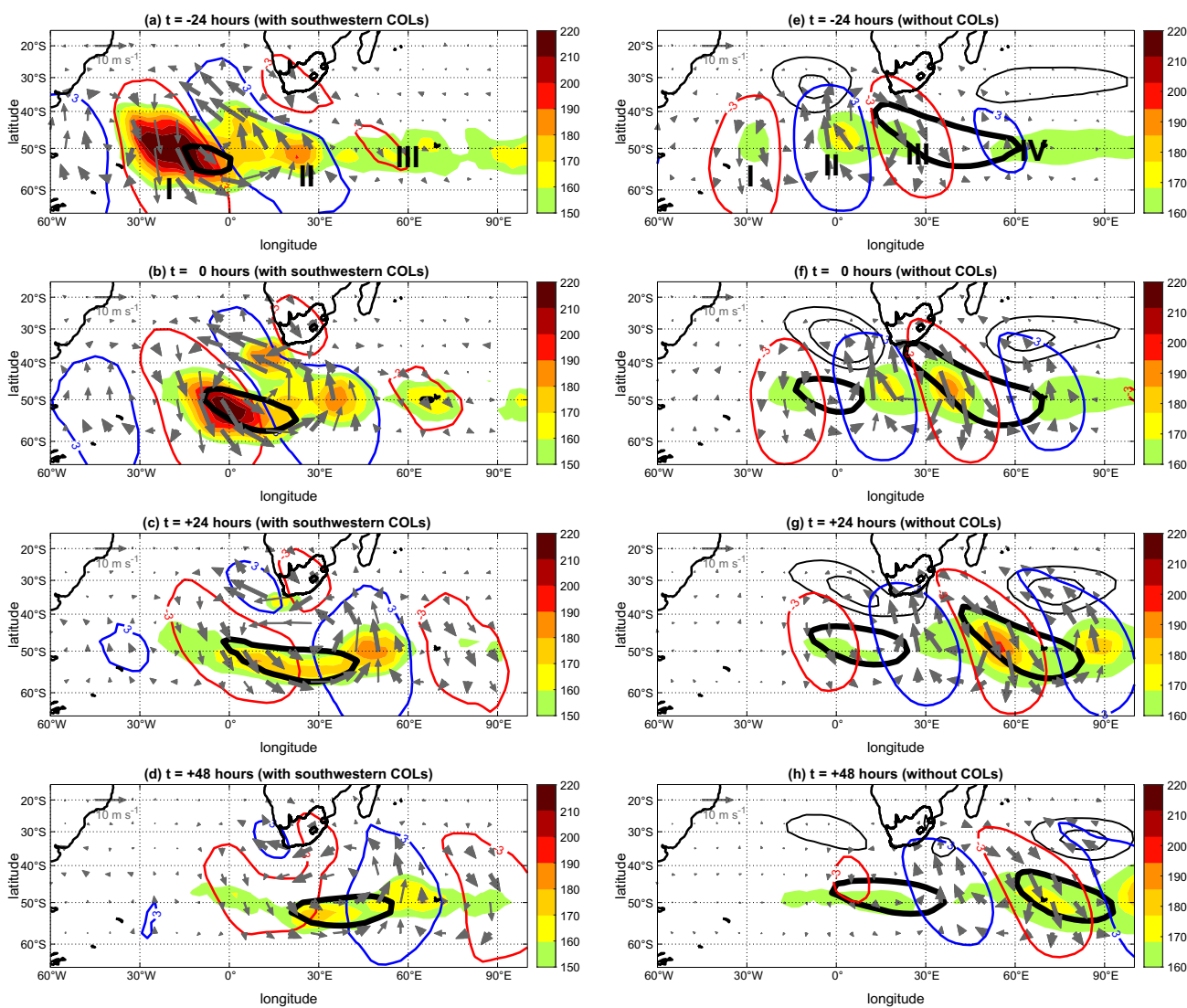
Fig. 6 Same as in Fig. 2 but for but for K_e (shaded) with values $K_e \geq 150$ m^2 s^{-2} shown, the perturbation flow (**v**, grey vectors). The thick arrows indicate indicate where the eddy flow vectors are significant at the 95% confidence levels. The thick solid black contours represent $U = 40$ m 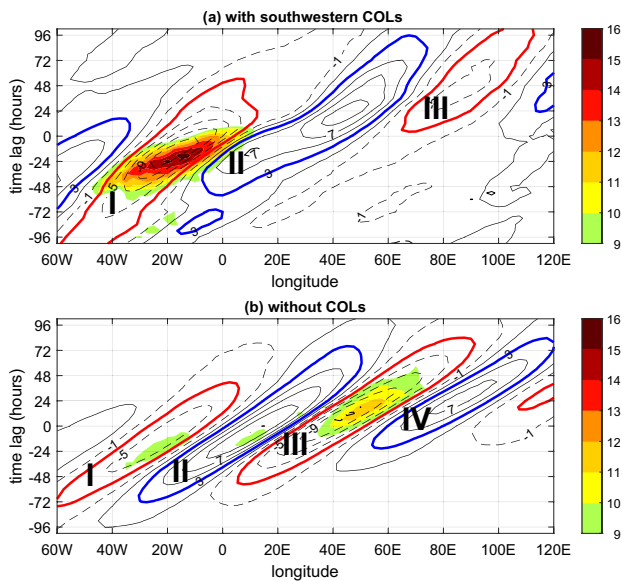s^{-1} isotach, to highlight the locattion of jet streaks. The thick solid red and blue contours represent $v = -3$ m s^{-1} and $+3$ m s^{-1}, resepctively, as in Fig. 4. The components of the baroclinic wave that propagate past the South African domain during ridging are labelled with Roman numerals I, II and III in the top panels, as in Fig. 4. In the right panels the eastern most eddy is labelled IV

much weaker, but are stronger across the trough, where the subgeostrophic flow is stronger than the same for COLs. Again, the relatively stronger easterly ageostrophic flow combined with the relatively stronger negative anomalies, lead to a more clearly defined flux field, across the trough axis between II and III in the right panels of Fig. 8. For this reason, $-\nabla \cdot (\mathbf{v}\phi)_a < 0$ is stronger in II when there are no COLs in the South African domain, instead of eddy I. Note that there is also energy transfer across the ridge between III and IV, so that the latter grows by means of downstream development, as suggested by the growth of K_e. Finally, Fig. 9 shows the Reynolds stress term, which may be decomposed into the barotropic and baroclinic conversions of K_e

to mean kinetic energy (Rivière et al. 2015), which signals the dissipation of the wave. This term is dominated by the former and is concentrated in eddy II for COLs but is located in component IV for the case of ridging highs without COLs. This is different from what Wirth et al. (2018) suggest. In that study, they proposed that baroclinic conversion occurs at the rear end of a wave packet.

4.4 Discussion of downstream development characteristics

In Sects. 4.1 and 4.2 it was shown that there are very clear differences in the flow across the ridge and trough axes

Fig. 7 Hovmöller diagrams of the composite meridional perturbation velocity v (thin black contours) and baroclinic conversion from eddy available potential energy to eddy kinetic energy ($-\omega\alpha > 0$, shaded) plotted in 1×10^4 m^2 s^{-3} for (**a**) south-western, (**b**) ridging highs without COLs. The solid (dashed) black contours represent the positive (negative) v values plotted at 2 m s^{-1} contour intervals and the thick solid red and blue contours highlight $v = -3$ m s^{-1} and $+3$ m s^{-1}, resepctively, as in Fig. 4. The components of the baroclinic wave that propagate past the South African domain during ridging are labelled with Roman numerals I, II and III in the top panels, as in Fig. 4. In the bottom panel the eastern most eddy is labelled IV

between the two categories of events. The supergeostrophic and subgeostrophic flows are respectively stronger for the cases of ridging with COLs and ridging without COLs. These differences are due to the PV anomaly structures that induce the flow which are associated with the jet streak structures. In turn, the characteristics of ageostrophic geopotential fluxes, and their divergence patterns, shown in Fig. 8, arise. Downstream development is best explained in terms of (1) the behaviour of K_e of the different eddies of a baroblinic wave and (2) downstream energy transfer by means of ageostrophic geopotential fluxes ($\mathbf{v}_a\phi$) and their divergence and convergence patterns.

Beginning with the evolution of K_e, it is shown in Fig. 9a that the eddy kinetic energy I (green curve) grows in a parabolic fashion to maximise at about 24 h before the formation of the COLs, as found to be the case by Ndarana et al. (2021b). The energy grows by means of converting eddy available potential energy, as Fig. 7 demonstrates. The blue curve in Fig. 9a shows that the eddy kinetic energy II also grows, but starts gradually at first and then more steeply when the one upstream has saturated. Furthermore it grows to surpass the maximum that eddy kinetic energy attains and then saturates at t = 0 h, when the COLs form. The facts that (1) there is no significant baroclinic conversion associated

with the eddy marked II in Fig. 7 and (2) there is no significant barotropic conversion in eddy I in Fig. 10 are together a clear indication that eddy II can only grow at the expense of eddy I, according to Eqs. (1) and (2), by means of transridge ageostrophic geopotential fluxes (Gan and Piva 2013; Ndarana et al. 2021b; Pinheiro et al. 2022), as suggested above. Note that the structure of the green curve (upstream eddy) vs. blue (downstream eddy) graphs in Fig. 9a is similar to Orlanski and Sheldon (1995) (cf. their Fig. 1a). The down turn in eddy kinetic energy II, beyond the formation of COLs, is caused by barotropic conversion (Fig. 10a).

The dynamical issues associated with the above, and the differences of these dynamics between COLs and ridging events that occur without COLs have already been discussed. For one thing, the supergeostrophic and subgeostrophic flow strengths are different because of the differences in the PV anomalies that induce it. The most significant downstream development processes occur downstream between eddies II and III across the trough, as the structure of the blue curve relative to the red one in Fig. 10b indicates. The fact that the growth of eddy I and II grow to maximise at lower values of K_e compared to when there COLs aloft is consistent with the weaker baroclinic conversion found there. Eddy III also grows from baroclinic conversion, but dissipates through trans-ridge downstream development in the Indian Ocean, after the commencement of the ridging process. This downstream energy transfer gives rise to the growth of eddy IV, which does not have a counterpart during COLs. Eddy IV can only grow from energy transferred from eddy III because the former has no baroclinic conversion associated with it (Fig. 7b). It dissipates via barotropic processes as clearly indicated in Fig. 10e. It follows from this discussion that downstream development during COLs occurs upstream so that energy in transferred from the midlatitudes into the South African domain, whilst when ridging high occur without COLs aloft, it occurs further downstream as the associated baroclinic wave propagates past the South African domain.

5 Concluding remarks

Using ERA 5 reanalysis data and building on Gan and Piva (2013), Ndarana et al. (2021b) and Pinheiro et al. 2022, this study shown that the behaviour of energy transfer in the South Atlantic Ocean/South African/Indian Ocean sector differs between days when there are COLs affecting South Africa and when they do not form during ridging high pressure systems. Figure 11 summarises these findings. The use of composite analysis in a geographic context shows that very strong baroclinic conversion occurs west of the Greenwich Meridian during COL pressure systems (indicated by the letters VS-BCC in Fig. 11a), and it is much stronger
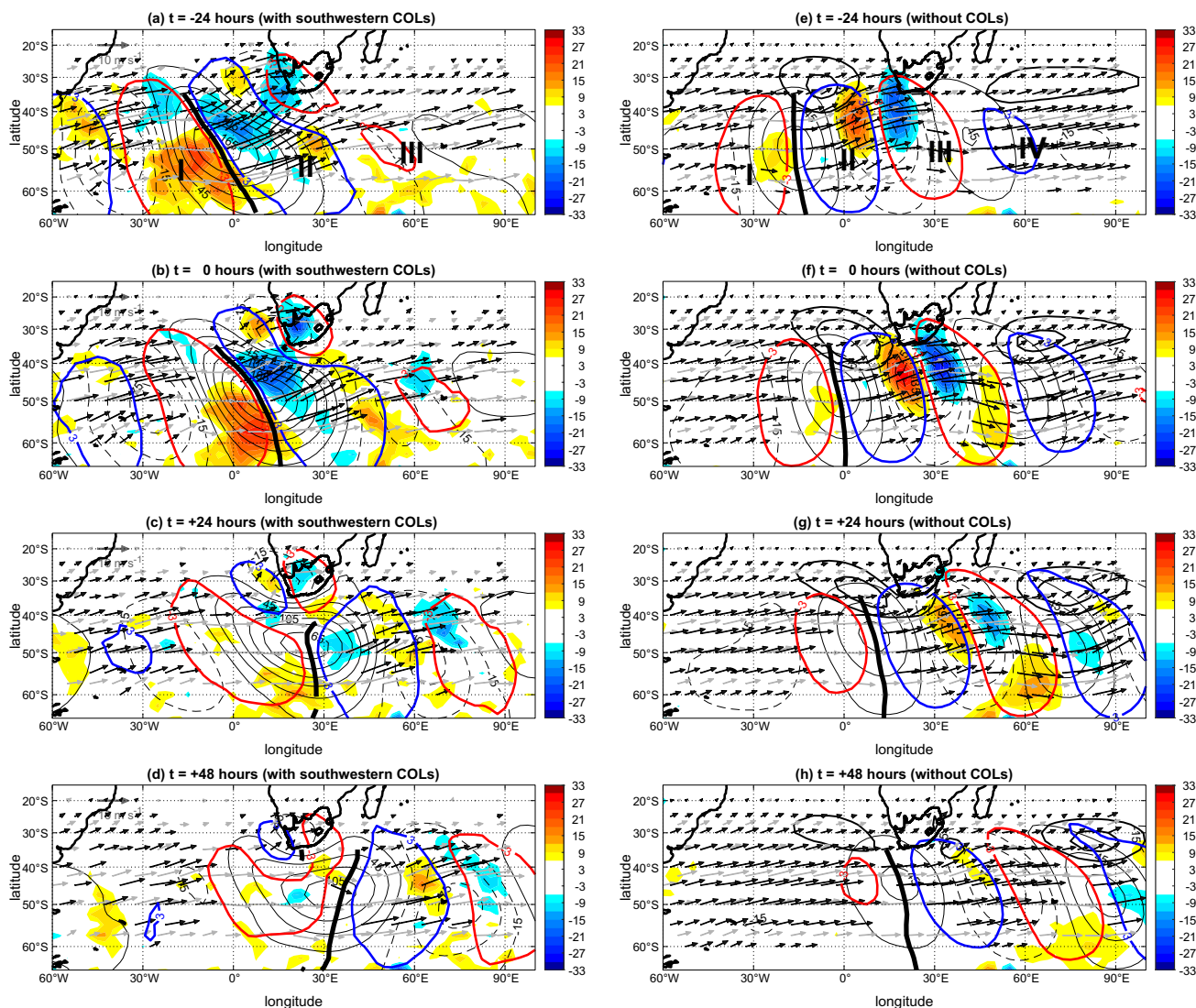
Fig. 8 Same as in Fig. 2 but for $-\nabla \cdot (\mathbf{v}\phi)_a$ (shaded) plotted in 1×10^4 m^2 s^{-3} and the geopotential height anomalies are plotted in 30 gpm contour intervals and the arrows represent $(\mathbf{v}_a\phi)$. The black arrows are statistically significant at the 95% confidence level

than when there are no COLs and it is found in eddy I (indicated by the letters W-BCC in Fig. 11d and e). By way of contrast, the weaker upstream baroclinic conversion found when no COLs occur during the ridging process but we also observe a slightly stronger conversion field in eddy II downstream of South Africa (indicated by the letters S-BCC in Fig. 11e), which appears to start occurring as the ridging process begins. Baroclinic conversion appears to generally occur at the rear end of the waves, which is consistent with Fig. 10 in Wirth et al. (2018). However, what this study has found is that barotropic conversion occurs downstream (i.e. eddy II in the case of COLs and eddy IV when there are no COLs, as indicated by the letters BTC ub Fig. 11c and f, respectively).

The differences in the energy transfer associated with these contrasting atmospheric conditions are due to the differences in the prevailing upper level dynamical processes. As Pinheiro et al. (2022) noted, baroclinic conversion occurs in the thermally direct region of the jet streaks embedded in the baroclinic waves. This jet streak is much stronger for COLs, hence the stronger baroclinic conversion. The presence of the baroclinic conversion downstream from South Africa in eddy III is informed by the presence of the downstream jet, which does not have a counterpart in that when COLs occur. Relative position composite fields in Ndarana and Waugh (2010), Ndarana et al. (2021b) and Pinheiro et al. (2022) suggest that it would be located over the South African mainland as suggested Fig. 11b. The stronger jet associated with COLs causes an increase the rate of strain, which
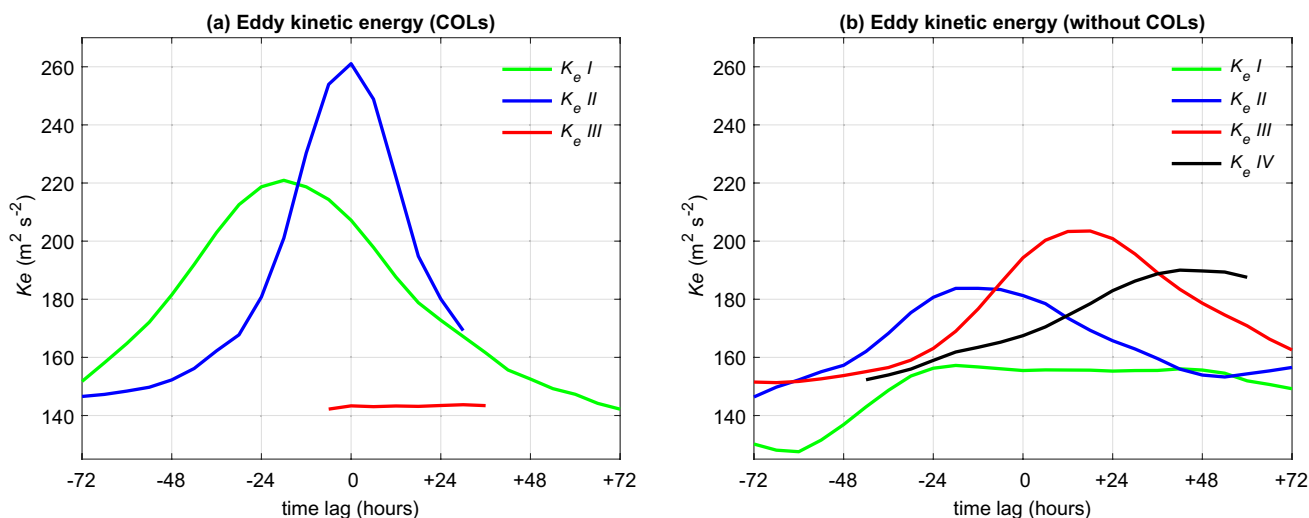
Fig. 9 Composite evolution of maximum eddy kinetic nergy during (**a**) all COL events (**b**) ridgng events when there are no COLs aloft. In both panels the green, blue and red curves represent the eddy kinetic energy of eddies I, II and III. In the left panel the black curve is the energy of component IV
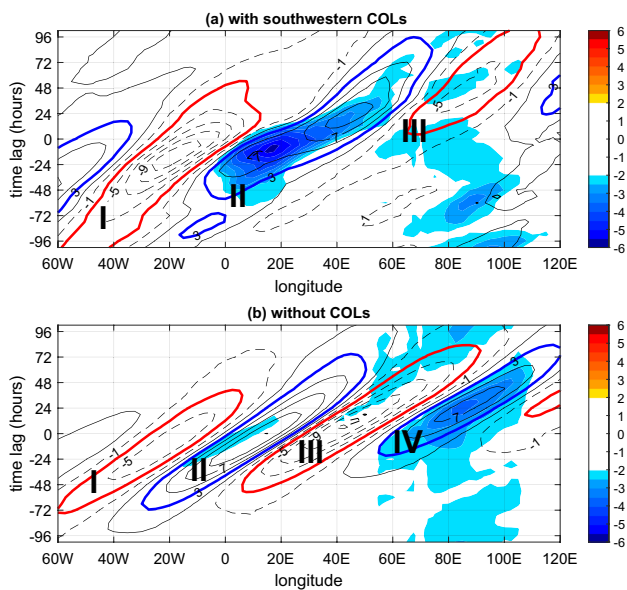
Fig. 10 Same as Fig. 7 but for $-\mathbf{v} \cdot (\mathbf{u} \cdot \nabla_p)\mathbf{V}_m$ (shaded) plotted in 1×10^4 m^2 s^{-3}

then causes the waves to break anticyclonically (Nakamura and Plumb 1994), in the vicinity of the Greenwich Meridian. The breaking has no counterpart when COLs do not form, because the upstream jet streak is weak. The breaking

and lack thereof then leads to stronger ageostrophic geopotential fluxes (as indicated by the double red curved red arrows in Fig. 11b), which are oriented so that they transport eddy kinetic energy in a north-easterly direction towards South Africa. The strong supergeostrophic flow is induced by the stronger geopotential height anomalies, which do not materialise during ridging highs, when COLs do not form. Even though the trans-trough axis (dashed line in Fig. 11e) downstream energy transport is weaker than when there is breaking, it is stronger than its upstream counterpart. This is largely due to the fact that the downstream jet in Fig. 11e marked "DJ" extends westward so that its entrance, and thus the negative relative vorticity anomaly at its entrance increases the negative anomalies of across the trough axis. This causes downstream propagation of the wave because it causes eddy III to grow, which itself dissipates by transferring energy into eddy IV by means of downstream development across the downstream ridge axis. The findings in this paper will have implications for medium range forecasting (MRF) time scale predictability studies of ridging highs and COLs in the South African domain. One way these findings could be implemented in the South African domain is to characterise downstream development in MRF ensemble systems to indicate whether or affirm that a COL is looming or not using the dynamical characteristics identified in this study.
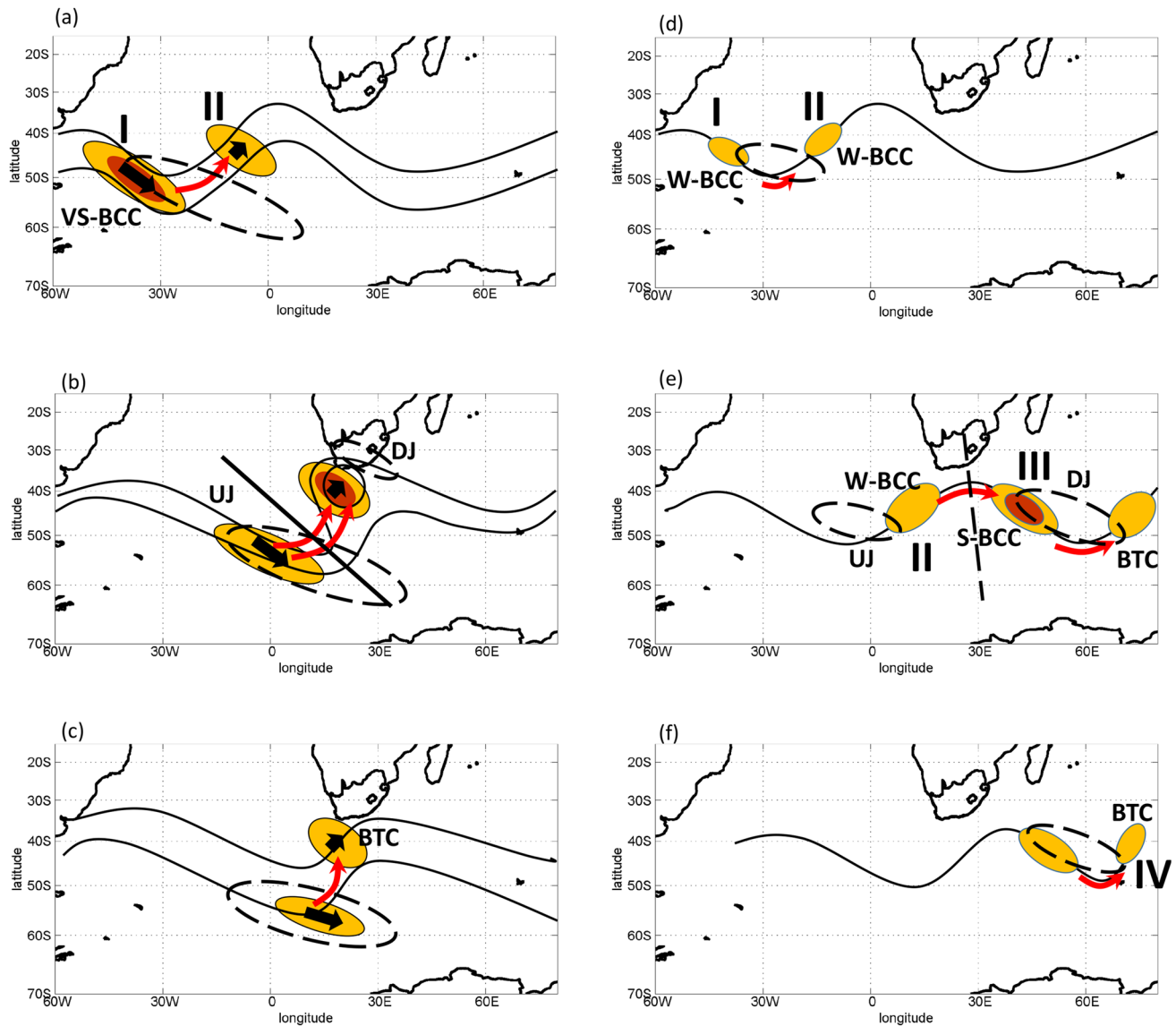
Fig. 11 Schematic of K_e during the evolution of COLs (left panels) and when there are no COLs (right panels) in the South African domain. The yellow and brown oval shapes represent the K_e, with the brown shade representing higher values of K_e. The dashed oval shapes represent the jet streaks. Areas marked W-BCC, S-BCC and VS-BCC indicate where weak, strong and very strong baroclinic conversion is located, respectively. The curved red arrows represent the ageostrophic geopotential fluxes and BTC represents where barotropic conversion is located. The eddies are labelled according to the schematic in Fig. 1

Author contributions TN, LEL and TSR conceptualised the research and TN prepared the schematics Figs. 1 and 11 and prepared the first draft of the manuscripts. LEL and TSR prepared the rest of the plots. All the authors contributed to the analysis and reviewed the manuscript.

Declaration

Conflict of interest The authors neither have conflict of interest nor competing interests.

References

Akahori K, Yoden S (1997) Zonal flow vacillation and bimodality of baroclinic eddy life cycles in simple global circulation model. J Atmos Sci 54:2351–2361. https://doi.org/10.1175/1520-0469(1997)054<2349:ZFVABO>2.0.CO;2

Barnes MA, Ndarana T, Landman W (2021) Cut' off lows in the Southern Hemisphere and their extension to the surface. Clim Dyn 56:3709–3732. https://doi.org/10.1007/s00382-021-05662-7

Blackburn W (1985) Interpretation of ageostrophic winds and implications for jet stream maintenance. J Atmos Sci 23:2604–2620. https://doi.org/10.1175/1520-0469(1985)042<2604:IOAWAI>2.0.CO;2

Brown TJ, Hall BL (1999) The use of t values in climatological composite analyses. J Clim 12:2941–2944. https://doi.org/10.1175/1520-0442(1999)012<2941:TUOTVI>2.0.CO;2

Chang EKM (2000) Wave packets and life cycles of troughs in the upper troposphere: examples from the Southern Hemisphere summer season of 1984/85. Mon Weather Rev 128:25–50. https://doi.org/10.1175/1520-0493(2000)128<0025:WPALCO>2.0.CO;2

Cook C, Reason CJC, Hewitson BC (2004) Wet and dry spells within particularly wet and particularly dry summers in the South African summer rainfall region. Clim Res 26:17–31. https://doi.org/10.3354/cr026017

Cook KH (1999) Generation of the African Easterly jet and its role in determining west Africa. J Clim 12:1165–1183. https://doi.org/10.1175/1520-0442(1999)012.3C1165:GOTAEJ.3E2.0.CO;2

Crétat J, Pohl B, Dieppois B, Berthou S, Perguad J (2019) The Angola Low: relationship with southern African rainfall and ENSO. Clim Dyn 52:1783–1803. https://doi.org/10.1007/s00382-018-4222-3

Danielson RE, Gyakum JR, Straub D (2006) A case study of downstream baroclinic development over the North Pacific Ocean. Part II: diagnoses of eddy energy and wave activity. Mon Weather Rev 134:1549–1567. https://doi.org/10.1175/MWR3173.1

D'Abreton PC, Tyson PD (1995) Divergent and non-divergent water vapour transport over southern Africa during wet and dry conditions. Meteorol Atmos Phys 55:47–59. https://doi.org/10.1007/BF01029601

De Kock WM, Blamey RC, Reason CJC (2021) Large summer rainfall events and their importance in mitigating droughts over the South Western Cape, South Africa. J Hydrometeorol 22:587–599. https://doi.org/10.1175/JHM-D-20-0123.1

de Vries AJ (2021) A global climatological perspective on the importance of Rossby wave breaking and intense moisture transport for extreme precipitation events. Weather Clim Dyn 2:129–161

Decker SG, Martin JE (2005) A local energetics analysis of the life cycle differences between consecutive, explosively deepening, continental cyclones. Mon Weather Rev 133:295–316. https://

doi.org/10.1175/1520-0442(1999)012$<$1165:GOTAEJ$>$2.0.CO;2

Dyson L (2015) A heavy rainfall sounding climatology over Gauteng, South Africa, using self-organising maps. Clim Dyn 45:3051–3065. https://doi.org/10.1007/s00382-015-2523-3

Engelbrecht CJ, Landman WA, Engelbrecht FA, Malherbe J (2015) A synoptic decomposition of rainfall over the Cape south coast of South Africa. Clim Dyn 44:2589–2607. https://doi.org/10.1007/s00382-014-2230-5

Engelbrecht FA, McGregor JL, Engelbrecht CJ (2009) Dynamics of the conformal-cubic atmospheric model projected climate-change signal over southern Africa. Int J Climatol 29:1013–1033. https://doi.org/10.1002/joc.1742

Fauchereau N, Pohl B, Reason CJC, Rouault M, Richard Y (2009) Recurrent daily OLR patterns in the Southern Africa/Southwest Indian Ocean region, implications for South African rainfall and teleconnections. Clim Dyn 32:575–591. https://doi.org/10.1007/s00382-008-0426-2

Gan MA, Piva ED (2013) Energetics of a Southeastern Pacific cut-off low. Atmos Sci Let 14:272–280. https://doi.org/10.1002/asl2.451

Gan MA, Piva ED (2016) Energetics of a Southeastern Pacific cut-off lows. Clim Dyn 46:3453–3462. https://doi.org/10.1007/s00382-015-2779-7

Harr PA, Dea JM (2009) Downstream development associated with the extratropical transition of tropical cyclones over the western North Pacific. Mon Weather Rev 137:1295–1319. https://doi.org/10.1175/2008MWR2558.1

Hart NCG, Reason CJC, Fauchereau N (2010) Tropical-extratropical interactions over southern Africa: three cases of heavy summer season rainfall. Mon Weather Rev 138:2608–2623. https://doi.org/10.1175/2010MWR3070.1

Hersbach H, Bell B, Berrisford P, Hirahara S, Horanyi A, Munoz-Sabater J, Nicolas J, Peubey C, Radu R, Schepers D, Simmons A, Soci C, Abdalla S, Abellan X, Balsamo G, Bechtold P, Biavati G, Bidlot J, Bonavita M, De Chiara G, Dahlgren P, Dee D, Diamantakis M, Dragani R, Flemming J, Forbes R, Fuentes M, Geer A, Haimberger L, Healy S, Hogan RJ, Holm E, Janiskova M, Keeley S, Laloyaux P, Lopez P, Lupu C, Radnoti G, de Rosnay P, Rozum I, Vamborg F, Villaume S, Thepaut J-N (2020) The ERA5 global reanalysis. QJR Meteorol Soc 146:1999–2049. https://doi.org/10.1002/qj.3803

Holton JR, Hakim GJ (2014) An Introduction to Dynamic Meteorology. 4th edn Elsevier Academic Press, pp 553. https://doi.org/10.1119/1.1987371

Hoskins BJ, McIntyre ME, Robertson AC (1985) On the use and significance of isentropic potential vorticity maps. QJR Meteorol Soc 111:877–946. https://doi.org/10.1002/qj.49711147002

Howard E, Washington R (2018) Characterizing the synoptic expression of the Angola Low. J Clim 31:7147–7165. https://doi.org/10.1175/JCLI-D-18-0017.1

Ivanciu I, Ndarana T, Matthes K, Wahl S (2022) On the ridging of the South Atlantic Anticyclone over South Africa: the impact of Rossby wave breaking and of climate change. Geophys Res Lett 49:e2022GL099607. https://doi.org/10.1029/2022GL099607

Keyser D, Shapiro MA (1986) A review of the structure and dynamics of upper-uevel frontal zones. Mon Weather Rev 114:452–499. https://doi.org/10.1175/1520-0493(1986)114$<$0452:AROTSA$>$2.0.CO;2

Lackmann GM, Keyser D, Bosart LF (1999) Energetics of an intensifying jet streak during the Experiment on Rapidly Intensifying Cyclones over the Atlantic (ERICA). Mon Wea Rev 127:2777–2795. https://doi.org/10.1175/1520-0493(1999)127$<$2777:EOAIJS$>$2.0.CO;2

Li X (2021) Maintenance of the South Asian jet wave train: eddy kinetic energy balance. Clim Dyn 57:687–700. https://doi.org/10.1007/s00382-021-05735-7

Macron C, Pohl B, Richard Y (2014) How do tropical temperate troughs form and develop over southern Africa. J Clim 27:1633–5199. https://doi.org/10.1175/JCLI-D-13-00175.1

McIntyre ME, Palmer TN (1983) Breaking planetary waves in the stratosphere. Nature 305:593–600. https://doi.org/10.1038/305593a0

McLay JG, Martin JE (2002) Surface cyclolysis in the North Pacific Ocean. Part III: composite local energetics of tropospheric-deep cyclone decay associated with rapid surface cyclolysis. Mon Weather Rev 130:2507–2529. https://doi.org/10.1175/1520-0493(2002)130$<$2507:SCITNP$>$2.0.CO;2

Müller GA, Gan MA, Piva ED (2017) Energetics of wave propagation leading to frost events in South America: extratropical latitudes. Atmos Sci Lett 18:342–348. https://doi.org/10.1002/asl.762

Nakamura M, Plumb RA (1994) The effects of flow asymmetry on the direction of Rossby wave breaking. J Atmos Sci 51:2031–2045. https://doi.org/10.1175/1520-0469(1994)051$<$2031:TEOFAO$>$2.0.CO;2

Ndarana T, Waugh DW (2010) The link between cut-off lows and Rossby wave breaking in the Southern Hemisphere. QJR Meteor Soc 136:869–885. https://doi.org/10.1002/qj.627

Ndarana T, Bopape M, Waugh D, Dyson L (2018) The influence of the lower stratosphere on ridging Atlantic Ocean anticyclones over South Africa. J Clim 31:6175–6187. https://doi.org/10.1175/JCLI-D-17-0832.1

Ndarana T, Mpati S, Bopape M, Engelbrecht FA, Chikoore H (2021) The flow and moisture fluxes associated with ridging South Atlantic Ocean anticyclones during the subtropical southern African summer. Int J Climatol 41:E1000–E1017. https://doi.org/10.1002/joc.6745

Ndarana T, Rammopo TS, Bopape M, Reason CJC, Chikoore H (2021) Downstream development during South African cut-off pressure systems. Atmos Res 249:105315. https://doi.org/10.1016/j.atmosres.2020.105315

Ndarana T, Rammopo TS, Chikoore H, Barnes MA, Bopape M (2020) A quasigeostrophic diagnosis of cut-off low pressure systems over South Africa and surrounding ocean. Clim Dyn 55:2631–2644. https://doi.org/10.1007/s00382-020-05401-4

Ndarana T, Rammopo TS, Reason CJC, Bopape M, Engelbrecht FA, Chikoore H (2022) Two types of ridging South Atlantic Ocean anticyclones over South Africa and associated dynamical processes. Atmos Res 265:105897. https://doi.org/10.1016/j.atmosres.2021.105897

O'Brien L, Reeder MJ (2017) Southern Hemisphere summertime Rossby waves and weather in the Australian region. QJR Meteor Soc 143:2374–2388. https://doi.org/10.1002/qj.3090

Orlanski I, Katzfey J (1991) The life cycle of a cyclone wave in the Southern Hemisphere. 1. Eddy energy budget. J Atmos Sci 48:1972–1998. https://doi.org/10.1175/1520-0469(1991)048<1972:TLCOAC>2.0.CO;2

Orlanski I, Sheldon J (1993) A case of downstream baroclinic development over western North America. Mon Wea Rev 121:2929–2950. https://doi.org/10.1175/1520-0493(1993)121$<$2929:ACODBD$>$2.0.CO;2

Orlanski I, Sheldon J (1995) Stages in the energetics if baroclinic systems. Tellus 47A:605–628. https://doi.org/10.1034/j.1600-0870.1995.00108.x

Peters D, Waugh DW (1996) Influence of barotropic shear on the poleward advection of upper-tropospheric air. J Atmos Sci 53:3013–3031. https://doi.org/10.1175/1520-0469(1996)053$<$3013:IOBSOT$>$2.0.CO;2

Pinheiro HR, Hodges KI, Gan MA, Ferreira SHS, Andrade KM (2022) Contributions of downstream baroclinic development to strong Southern Hemisphere cut-off lows. QJR Meteorol Soc 148:214–232. https://doi.org/10.1002/qj.4201

Pinto I, Zachariah M, Wolski P, Landman S, Phakula V, Maluleke W, Bopape M, Engelbrecht C, Jack C, McClure A, Bonnet R, Vautard R, Philip S, Kew S, Heinrich D, Vahlberg M, Singh R, Arrighi1 J, Thalheimer L, van Aalst1 M, Li11 S, Sun J, Vecchi G, Yang W, Tradowsky J, Otto FEL, Dipura1 R (2022) Climate change exacerbated rainfall causing devastating flooding in Eastern South Africa. World Weather Attribution. https://www.worldweatherattribution.org/wp-content/uploads/WWA-KZN-floods-scientific-report.pdf Accessed 31 July 2022

Piva ED, Gan MA, Rao VB (2008) An Objective Study of 500-hPa Moving Troughs in the Southern Hemisphere. Mon Wea Rev 136:2186–2200. https://doi.org/10.1175/2007MWR2135.1

Piva ED, Gan MA, Rao VB (2010) Energetics of Winter Troughs Entering South America. Mon Wea Rev 138:1084–1103. https://doi.org/10.1175/2009MWR2970.1

Portmann R, Sprenger M, Wernli H (2021) The three-dimensional life cycles of potential vorticity cutoffs: a global and selected regional climatologies in ERA-Interim (1979–2018). Weather Clim Dynam Discuss 2:507–534. https://doi.org/10.5194/wcd-2-507-2021

Rapolaki RS, Blamey RC, Hermes JC, Reason CJC (2020) Moisture sources associated with heavy rainfall over the Limpopo River basin, southern Africa. Clim Dyn 55:1473–1487. https://doi.org/10.1007/s00382-020-05336-w

Ratna SB, Behera S, Ratnam JV, Takahashi K, Yamagata T (2013) An index for tropical temperate troughs over southern Africa. Clim Dyn 41:421–441. https://doi.org/10.1007/s00382-012-1540-8

Reason CJC (2000) Multidecadal climate variability in the subtropics/midlatitudes of the Southern Hemisphere oceans. Tellus A Dyn Meteorol Oceanogr 52(2):203–223. https://doi.org/10.3402/tellusa.v52i2.12259

Reason C, Jagadheesha D (2005) A model investigation of recent ENSO impacts over southern Africa. Meteorol Atmos Phys 89:181–205. https://doi.org/10.1007/s00703-005-0128-9

Reboita MS, Ambrizzi T, Silva BA, Pinheiro RF, da Rocha RP (2019) The South Atlantic subtropical anticyclone: Present and future climate. Front Earth Sci 7:8. https://doi.org/10.3389/feart.2019.00008

Reyers M, Shao Y (2019) Cut off lows off the coast of the Atacama Desert under present day condition and in the Last Glacial Maximum. Global Planet Chang 181:102–983. https://doi.org/10.1016/j.gloplacha.2019.102983

Rivière R, Arbogast P, Joly A (2015) Eddy kinetic energy redistribution within windstorms Klaus and Friedhelm. QJR Meteorol Soc 141:925–938. https://doi.org/10.1002/qj.2412

Røsting B, Kristjánsson JE (2012) The usefulness of piecewise potential vorticity inversion. J Atmos Sci 69:1520–0469. https://doi.org/10.1175/JAS-D-11-0115.1

Singleton AT, Reason CJC (2007) A numerical study of an intense cut-off low pressure system over South Africa. Mon Wea Rev 135:1128–1150. https://doi.org/10.1175/MWR3311.1

Singleton AT, Reason CJC (2016) Numerical simulations of a severe rainfall event over the Eastern Cape coast of South Africa: sensitivity to sea surface temperature and topography. Tellus A Dyn Meteorol Oceanogr 58:335–367. https://doi.org/10.1111/j.1600-0870.2006.00180.x

Sun X, Cook KH, Vizy EK (2017) The South Atlantic subtropical high: Climatology and interannual variability. J Clim 30:3279–3296. https://doi.org/10.1175/JCLI-D-16-0705.1

Taljaard JJ (1985) Cut-off lows in the South African region. South African Weather Bureau Technical Paper 14, 153. [Available from the South African Weather Service, Private Bag x097, Pretoria, 0001, South Africa.]

Thoithi W, Blamey R, Reason C (2023) April 2022 Floods over East Coast South Africa: interactions between a mesoscale convective system and a coastal meso-low. Atmosphere 14:78. https://doi.org/10.3390/atmos14010078

Thorncroft CD, Hoskins BJ, McIntyre ME (1993) Two paradigms of baroclinic-wave life-cycle behaviour. 119:17–55. https://doi.org/10.1002/qj.49711950903

Trigaardt DO, Terblanche DE, van Heerden J, Laing MV (1988) The Natal flood of September 1987. South African Weather Bureau Tech Paper 19 pp 62. [Available from the South African Weather Service, Private Bag x097, Pretoria, 0001, South Africa.]

Uccellini LW, Kocin PJ (1987) The interaction of jet streak circulations during heavy snow events along the east coast of the United States. Weather Forecasting 2:289–308. https://doi.org/10.1175/1520-0434(1987)002$<$0289:TIOJSC$>$2.0.CO;2

Vigaud N, Richard Y, Rouault M, Fauchereau N (2007) Water vapour transport from the tropical Atlantic and summer rainfall in tropical southern Africa. Clim Dyn 28:113–123. https://doi.org/10.1007/s00382-006-0186-9

Weldon D, Reason CJC (2014) Variability of rainfall characteristics over the South Coast region of South Africa. Theor Appl Climatol 115:177–185. https://doi.org/10.1007/s00704-013-0882-4

Wirth V, Riemer M, Chang EKM, Martius O (2018) Rossby Wave Packets on the Midlatitude Waveguide-A Review. Mon Wea Rev 146:1965–2001. https://doi.org/10.1175/MWR-D-16-0483.1